Check for updates

Advanced Materials

ADVANCED MATERIALS
www.advmat.de

RESEARCH ARTICLE

Integrated Electrode-to-Device Design via Combination of Grain Boundary Reconstruction and Dynamic Gas Management Toward Stable 3 Ah Aqueous Zinc-Iodine Pouch Cells

Minghao Zhang | Ruibo Sun | Haowei Mo | Chenxi Sun | Hong Lin | Huadong Jiang | Jinbao Zhao | Yang Yang

State Key Laboratory of Physical Chemistry of Solid Surfaces, State-Province Joint Engineering Laboratory of Power Source Technology for New Energy Vehicle, College of Chemistry and Chemical Engineering, Xiamen University, Xiamen, P. R. China

Correspondence: Jinbao Zhao (jbzhao@xmu.edu.cn) | Yang Yang (yangyang419@xmu.edu.cn)

Received: 15 January 2026 | **Revised:** 31 March 2026 | **Accepted:** 17 June 2026

Keywords: Ah-level pouch cell | gas management | grain boundary reconstruction | H_2 expulsion | zinc-iodine battery

ABSTRACT

The substantial electrochemical performance gap between Ah-level pouch cells and laboratory-scale coin cells remains a critical bottleneck hindering the practical application of aqueous Zn-I_2 batteries. Herein, Zn anode degradation and cell-level gas accumulation, exacerbated under large-area-electrode conditions, are systematically identified as dominant failure mechanisms in high-capacity Zn-I_2 pouch cells. Accordingly, an integrated electrode-to-device strategy is proposed, combining Zn grain-boundary reconstruction with dynamic gas management. The intrinsically nonuniform grain boundary distribution in commercial zinc foil is confirmed to induce stripping heterogeneity and subsequent dendrite growth, while persistent H_2 evolution leads to cell swelling and electrolyte leakage, ultimately resulting in accelerated capacity fading. At the electrode level, a scalable electrodeposition strategy yields current-collector-integrated zinc anodes with refined grains and homogenized boundaries, effectively mitigating initial stripping heterogeneity and enhancing zinc utilization. At the device level, a selective H_2-expulsion window (LaNi-based hydrogen storage alloy nanoparticles embedded in a hydrophobic PTFE matrix) is integrated into the aluminum-plastic packaging, enabling efficient H_2 removal while blocking water vapor to maintain electrolyte stability. Leveraging this design, multilayer-stacked Zn-I_2 pouch cells with >3 Ah capacity and an ultra-low N/P ratio of 1.18 achieve over 600 stable cycles. This work offers a scalable, system-level solution toward practical aqueous Zn-based pouch cells.

1 | Introduction

Benefitting from the intrinsic safety of aqueous electrolytes, the low redox potential (−0.76 V vs. SHE) and high theoretical capacity (820 mAh g^{-1}) of Zn metal anodes, aqueous zinc metal batteries have emerged as a promising solution for large-scale energy storage applications [1–3]. Among them, aqueous zinc-iodine batteries are particularly attractive due to the favorable characteristics of iodine cathodes, including a suitable redox potential (~0.536 V vs. SHE), high theoretical capacity (211 mAh g^{-1}), and natural abundance (55 μg L^{-1} in ocean) [4, 5]. The pouch-cell format, featuring lightweight and robust aluminum-plastic film packaging, has become a key enabler for Zn-I_2 batteries' commercialization owing to its high spatial efficiency, customizable geometry, and compatibility with stackable architectures [6–8]. However, scaling from laboratory-scale coin

© 2026 Wiley-VCH GmbH

cells to practical ampere-hour (Ah)-level pouch cells imposes significant challenges, including substantially larger electrode areas, higher active material loadings, and reduced stack pressures, all of which intensify the risk of battery failure [9, 10]. Encouragingly, recently reported advanced dry-processing routes for iodine cathode [11–13] have enabled the fabrication of high-loading, large-area electrodes with excellent uniformity, redox reversibility, and less polyiodide shuttling, thereby accelerating the pathway to practical Zn-I_2 batteries. At this stage, however, the reversibility and stability of the zinc anode have emerged as the primary bottlenecks constraining the advancement of Zn-I_2 pouch batteries. Especially under high-areal-capacity and large-area conditions typical of Ah-scale devices, pronounced non-uniform Zn stripping/plating and persistent hydrogen-evolution reaction (HER) severely compromise electrochemical performance (Figure 1a) [14, 15], motivating a re-evaluation of anode optimization strategies from a device-level, application-oriented perspective.

From the perspective of the Zn electrode, its deposition behavior is governed by two critical factors: (i) process-related parameters, including ion desolvation, diffusion, and nucleation kinetics, and (ii) the initial state of the substrate, encompassing surface morphology and intrinsic electrochemical activity [16–19]. Considerable progress has been made in optimizing these process-related factors through electrolyte engineering [20–23] and surface coatings [24–28], which have markedly improved Zn plating/stripping reversibility in coin-cell formats. However, their effectiveness deteriorates substantially in larger-format pouch cells (Figure 1c and Table S1). This scale-dependent performance gap indicates that non-uniformities in the initial Zn substrate state become the dominant failure mechanism under practical device configurations. Importantly, many zinc-based full cells (e.g., with I_2, V_2O_5, or MnO_2 cathodes) begin with a discharge step, corresponding to Zn stripping [4, 16, 29, 30]. Hence, the uniformity of this initial stripping process across large-area Zn electrodes is critical for ensuring stable long-term cycling [31, 32]. Although macroscopically smooth, commercial rolled Zn foil is polycrystalline and exhibits heterogeneous grain-boundary distribution [33–35]. Zn atoms located in regions with finer grains and higher boundary densities preferentially dissolve during the initial stripping, forming localized pits or even perforations that serve as nucleation sites for non-uniform Zn replating (Figure 1a) [11, 36]. In large-area pouch-cell electrodes, the statistical likelihood of such morphological defects increases, elevating the risk of internal short circuits [37]. Furthermore, reducing Zn foil thickness to achieve higher energy density (i.e., lower N/P ratio) further intensifies grain-boundary-driven inhomogeneous stripping, which exacerbates morphological instability, raises susceptibility to macroscopic failures (e.g., perforation or tab corrosion), and ultimately limits active-material utilization [37–39].

From the device-level perspective, the hydrogen evolution reaction (HER) remains a persistent and complex issue, particularly difficult to completely suppress during Zn electrodeposition due to the relatively low reduction potential of zinc [19, 40, 41]. In pouch-type cells, the substantially larger electrode area and higher operating current density markedly increase the gas evolution rate compared to coin cells. Owing to the absence of rigid mechanical support in pouch cells, rapidly generated gas causes swelling or even rupture, resulting in electrolyte leakage and capacity degradation [9, 42]. Moreover, localized hydrogen accumulation disrupts the electrode–electrolyte interface, raises local polarization, and aggravates non-uniform zinc deposition [43]. In fact, gas evolution has long posed a challenge for various aqueous battery systems. For instance, commercial valve-regulated lead-acid batteries employ pressure-relief valves to release excess gas [44]. Similarly, Yang et al. proposed an "open" Zn metal pouch cell to expel H_2 gas, mitigating gas-induced swelling and safety concerns [45]. However, unavoidable electrolyte loss in such open systems may degrade electrochemical performance and necessitate frequent water replenishment. Consequently, achieving uniform zinc deposition by homogenizing grain-boundary structures, together with implementing simple yet effective gas management strategies, constitutes a critical challenge in translating advancements in electrode design into practical pouch-cell implementation.

Herein, an integrated electrode-to-device design that couples grain boundary reconstruction with dynamic gas management is proposed to achieve long-term cycling stability in high-capacity aqueous Zn-I_2 pouch cells (Figure 1b). Using a dry-processed, high-loading iodine cathode (>5 mAh cm^{-2}) in an Ah-level pouch cell configuration, two primary anode-related failure modes are identified: dendrite-induced short circuits during early cycles and cell swelling/rupture caused by prolonged H_2 accumulation over extended operation (Figure 1a). At the electrode level, Zn anodes with refined grains and homogenized grain-boundary distribution are fabricated via a scalable electrodeposition process, enabling macroscopically uniform Zn stripping and subsequent reversible Zn cycling to eliminate short-term failure. Additionally, this process introduces a built-in current collector, which enhances mechanical integrity under high utilization and supports practical low-N/P configurations. To address hydrogen accumulation at the cell level, a selective H_2-expulsion window is designed and integrated into the aluminum-plastic packaging. This window consists of a hydrophobic PTFE scaffold and LaNi-based hydrogen storage alloy fillers, which enable active H_2 removal during cycling while effectively blocking water vapor and electrolyte leakage, ensuring internal gas management without compromising cell sealing. As a result, a stacked Zn-I_2 pouch cell with a high cell-level capacity (>3.3 Ah) demonstrates stable cycling over 600 cycles at an ultra-low N/P ratio of 1.18. Moreover, the proposed integrated electrode-to-device design is broadly compatible with further anode/electrolyte interfacial engineering and adaptable to various cathode chemistries, offering a system-level pathway for the practical realization of high-performance Zn-based pouch cells.

2 | Results and Discussion

2.1 | Realization of Uniform Large-Area Stripping Through Grain-Boundary Reconstruction

To investigate the failure mechanisms in large-format aqueous zinc pouch cells, Ah-level Zn||I_2 pouch full cells were assembled by pairing a single-layer zinc anode with a dry-processed, high-loading iodine cathode (>600 mAh), with a reserved gas chamber to eliminate gas-induced interference. As illustrated in Figure 2a, when a 100 μm-thick commercial zinc foil was employed as the

15214095, 2026, 45, Downloaded from https://advanced.onlinelibrary.wiley.com/doi/10.1002/adma.73914 by Xiamen University, Wiley Online Library on [08/11/2026]. See the Terms and Conditions (https://onlinelibrary.wiley.com/terms-and-conditions) on Wiley Online Library for rules of use; OA articles are governed by the applicable Creative Commons License

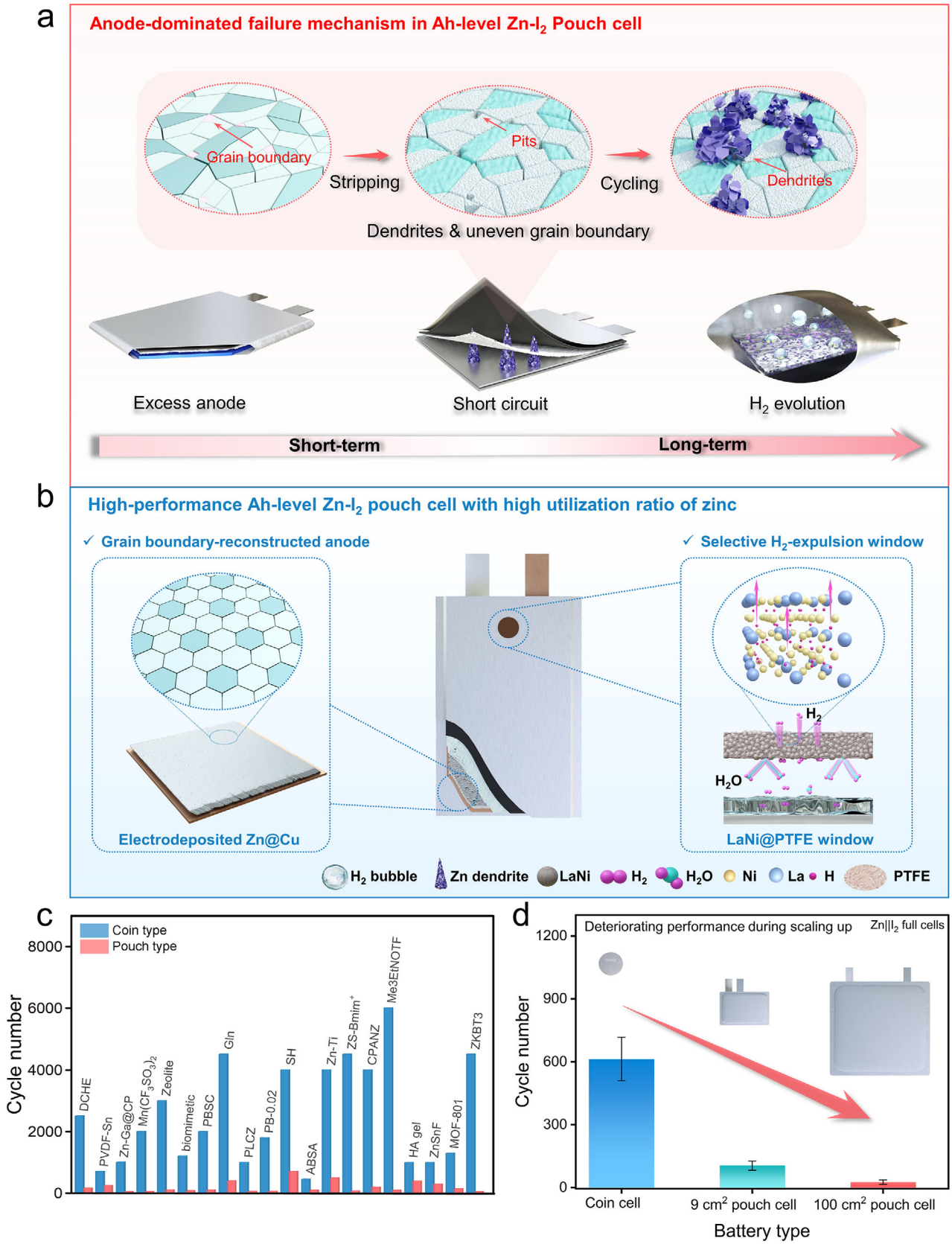

FIGURE 1 | Integrated electrode-to-device design for high-performance Ah-level Zn-I_2 pouch cells. (a) Schematic diagram of the failure mechanism for Ah-level pouch cells and the dendrite growth mechanism induced by uneven grain boundaries in commercial zinc foils. (b) Schematic diagram of the electrode-to-device design achieved through a grain-boundary-reconstructed anode and selective H_2-expulsion window. (c) Comparison of cycle life between coin-type and pouch-type cells with various material designs. (d) Deteriorating cycling performance of Zn||I_2 full cells with the same areal capacity of ~5 mAh cm^{-2} at 1 C upon scaling from coin-type to large-format pouch cells (data based on three cells).

15214095, 2026, 45, Downloaded from https://advanced.onlinelibrary.wiley.com/doi/10.1002/adma.73914 by Xiamen University, Wiley Online Library on [08/11/2026]. See the Terms and Conditions (https://onlinelibrary.wiley.com/terms-and-conditions) on Wiley Online Library for rules of use; OA articles are governed by the applicable Creative Commons License

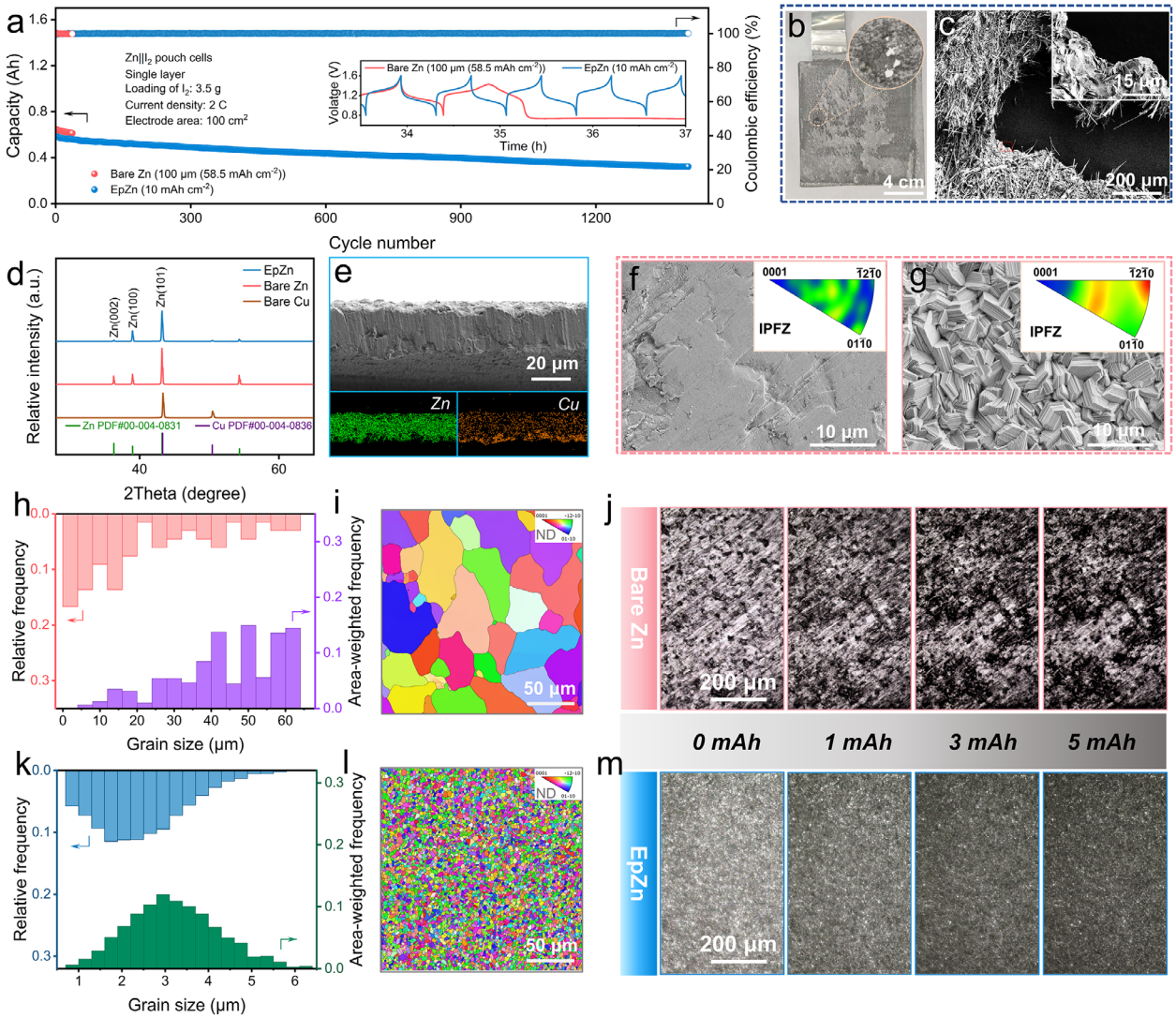

FIGURE 2 | Electrodeposited Zn anode with reconstructed grain boundaries. (a) Cyclic performance of Zn||I_2 pouch cells with different anodes. (Inset is the corresponding time-voltage curves). (b,c) (b) Photograph and (c) SEM images of failed commercial Zn foil after cycling. (d) XRD patterns of different anodes. (e) Cross-sectional SEM image and corresponding elemental mappings of the EpZn electrode. (f,g) SEM images and inverse pole figures of (f) commercial zinc foil and (g) EpZn electrode. (h–j) Characterization of commercial Zn foils: (h) grain size distribution, (i) inverse pole figure orientation map, and (j) in situ optical microscopy images during the stripping process at 20 mA cm^{-2}. (k–m) Characterization of EpZn electrodes: (k) grain size distribution, (l) inverse pole figure orientation map, and (m) in situ optical microscopy images during the stripping process at 20 mA cm^{-2}.

anode, the pouch cell experienced a rapid short circuit after only 36 cycles, as evidenced by a sudden voltage drop during charging, which occurred significantly earlier than that observed in coin cells or smaller pouch cells (Figure 1d and Figure S1). To further confirm that the failure originates from the anode side, the failed pouch cell was reassembled using the same cathode but with a fresh separator, electrolyte, and Zn anode. As presented in Figure S2, the reassembled cell successfully resumed operation, and the recovered cathode showed no structural degradation. In addition, obvious localized perforation was observed on the zinc foil anode (Figure 2b,c). Considering that the actual depth of discharge (DOD) of the 100 μm-thick commercial zinc foil is merely 11% in this pouch cell, the formation of such perforation underscores the severe aggravation of non-uniform stripping behavior in large-format electrodes, where localized degradation rapidly accumulates and leads to premature failure.

To address this issue, an electrodeposition strategy is employed to fabricate the zinc anodes with reconstructed grain boundaries. The 10 μm commercial copper foil is utilized as the substrate, and both complexing and leveling agents are introduced into the plating bath to promote electrodeposited Zn grain refinement and homogenization. Specifically, the formulation employs small-molecule, highly water-soluble, and chemically stable additives (citric acid and 2-methylimidazole) that can be readily removed by post-deposition rinsing, thereby avoiding severe additive residue contamination that could compromise subsequent cycling performance (Figures S3–S5). As shown in Figure 2e, the electrodeposited zinc (EpZn) forms a dense and flat layer tightly adhered to the copper substrate. Its surface features compact, uniformly sized zinc crystals with inclined orientation (Figure 2g). The inverse pole figure from electron backscatter diffraction (EBSD) measurement reveals that the EpZn anode possesses a predominant Zn (101) crystallographic orientation,

15214095, 2026, 45, Downloaded from https://advanced.onlinelibrary.wiley.com/doi/10.1002/adma.73914 by Xiamen University, Wiley Online Library on [08/11/2026]. See the Terms and Conditions (https://onlinelibrary.wiley.com/terms-and-conditions) on Wiley Online Library for rules of use; OA articles are governed by the applicable Creative Commons License

whereas the commercial Zn foil exhibits randomly oriented grains (Figure 2f), consistent with XRD results (Figure 2d). Moreover, even at a high deposition capacity of 20 mAh cm^{-2}, the EpZn maintains a dense and flat morphology and enables stable cycling (Figure S6), confirming the flexibility and reliability of this electrodeposition process and formulation.

Zn atoms at grain boundaries, characterized by incomplete coordination and less dense packing, exist in a higher energy state. Scanning Kelvin probe microscopy (SKPM) reveals that a higher surface potential (corresponding to a lower work function) boundary appears on an otherwise flat surface, confirming the presence of highly active grain boundaries (Figure S7). Density functional theory (DFT) calculations further show that the dissolution energy of Zn atoms at the center site of the crystal surface is much higher than that at the side or corner sites (Figure S8). This substantial decrease is attributed to the reduced coordination number at side and corner sites, confirming that Zn atoms at grain boundaries are preferentially oxidized during electrochemical stripping. Notably, the dissolution energies on the Zn (002) surface are generally higher than those on the Zn (101) surface, consistent with the known corrosion resistance of the (002) plane [46, 47]. Therefore, the Zn (101) orientation can facilitate faster Zn stripping/deposition kinetics, which is expected to offer uniform electrochemical behavior under high current densities. Grain boundary distributions are further analyzed by EBSD to assess their impact on stripping behavior. As shown in Figure 2h,i, the commercial Zn foil exhibits a broad and highly heterogeneous grain size distribution, ranging randomly from 1 to 60 μm. According to metal corrosion theory, regions with smaller grains, characterized by higher grain boundary density and surface energy, are more prone to preferential dissolution during stripping. Although small grains are numerically considerable in commercial Zn foil, their area-weighted proportion is minimal, making the electrode highly susceptible to localized perforation under high-capacity cycling conditions. In situ optical microscopy test (Figure 2j and Video S1) shows that stripping on the commercial Zn foil initiates with random pitting, which subsequently evolves into deep cavities. In contrast, the EpZn anode exhibits a narrow, near-normal grain size distribution (~2–5 μm) in both number-frequency and area-weighted plots (Figure 2k,l). In situ optical stripping tests confirm that the reconstructed homogeneous grain boundaries in EpZn enable macroscopically uniform stripping across the electrode surface (Figure 2m and Video S2). When coupled with a dry-processed I_2 cathode, the EpZn anode (10 mAh cm^{-2}) allows the pouch full cell to stably cycle for over 1400 cycles (Figure 2a). These results demonstrate that grain-boundary-induced stripping inhomogeneity is a critical root cause of rapid Zn anode failure in pouch cells, which can be effectively mitigated by grain-boundary reconstruction via the EpZn strategy.

2.2 | Intrinsic Correlation Between Grain Boundary Distribution and Cycling Performance

The influence of stripping-induced heterogeneity on subsequent zinc deposition and cycling behavior is systematically investigated. As presented in Figure 3a, commercial zinc foil (20 μm thick) with non-uniform grain boundaries displays highly uneven morphology after stripping 3 mAh cm^{-2} (Figure 3b). While most regions show negligible stripping traces, localized areas suffer from complete perforation (Figure 3b,c). During subsequent cycling, the newly deposited zinc preferentially accumulates around pit edges instead of refilling the voids, resulting in loosely adhered, randomly oriented dead zinc deposits (Figure 3d). Laser scanning confocal microscopy (LSCM) further confirms severe deposition inhomogeneity on the cycled Zn foil, with surface height variations reaching tens of micrometers (Figure 3e). This severe inhomogeneity stems from local current density fluctuations during stripping (Figure 3k), driven by the intrinsically non-uniform grain boundaries, which promote uneven dissolution and dendritic growth (Figure S9). In contrast, EpZn anodes with refined and homogeneous grains exhibit uniform current distribution (Figure 3f,l), enabling homogeneous large-area stripping and preserving good electrode structural integrity over repeated cycles (Figure 3g–i and Figure S10). LSCM results reveal that cycled EpZn surfaces remain remarkably flat, with height variations of only a few micrometers over a 620 μm × 620 μm area (Figure 3j), highlighting the effectiveness of grain boundary reconstruction in improving Zn stripping/deposition reversibility.

The increased grain boundary ratio and refined grains will enhance the exchange current density of the zinc redox reaction. As shown in Figure 3m, chronopotentiometry tests in a three-electrode system reveal lower overpotentials for both Zn deposition and stripping on the EpZn electrode. Chronoamperometry results (Figure S11) further demonstrate that the EpZn anode delivers higher and more stable response currents during the stripping process, which is beneficial for reducing electrode polarization during high-rate cycling.

To evaluate practical reversibility under high-utilization conditions, 20 μm zinc foil (11.7 mAh cm^{-2}) and limited-capacity EpZn (10 mAh cm^{-2}) are employed for the assembly of symmetric cells. As shown in Figure 3n, the bare Zn||Zn symmetric cell fails within 50 h at 10 mA cm^{-2} for 5 mAh cm^{-2}, while the EpZn||EpZn symmetric cell exhibits an extended cyclic life for over 400 h. At a higher current density of 25 mA cm^{-2} (Figure 3o), the bare Zn||Zn symmetric cell exhibits a sharp polarization increase after 80 h due to zinc exhaustion, whereas the EpZn||EpZn symmetric cell maintains stable cycling for over 200 h with a lower voltage hysteresis of 0.08 V. Under an even more demanding condition with a depth of discharge (DOD) of 75% (7.5 mAh cm^{-2}), the bare Zn||Zn symmetric cell rapidly exhibits a depletion-induced polarization surge due to severe structural collapse, while the EpZn||EpZn symmetric cell achieves stable operation for over 100 h (Figure S12). Rate performance tests further demonstrate that the EpZn||EpZn symmetric cell maintains stable cycling with low polarization across a wide current density range from 5 to 50 mA cm^{-2} (Figure S13). Under milder conditions (1 mA cm^{-2} for 1 mAh cm^{-2}), the EpZn||EpZn symmetric cell can sustain operation for over 3200 h (Figure S14), demonstrating the enhanced electrochemical reversibility of the EpZn anode under a broad range of current densities and deep discharge conditions. Importantly, the coarse EpZn with non-uniform grains (control sample), prepared without grain-refining additives (from pure $ZnSO_4$ electrolyte), fails within 60 h due to short-circuiting (Figures S15 and S16), emphasizing the critical synergistic mechanisms of the built-in current collector, grain-size refinement, and grain-boundary homogeniza-

15214095, 2026, 45, Downloaded from https://advanced.onlinelibrary.wiley.com/doi/10.1002/adma.73914 by Xiamen University, Wiley Online Library on [08/11/2026]. See the Terms and Conditions (https://onlinelibrary.wiley.com/terms-and-conditions) on Wiley Online Library for rules of use; OA articles are governed by the applicable Creative Commons License

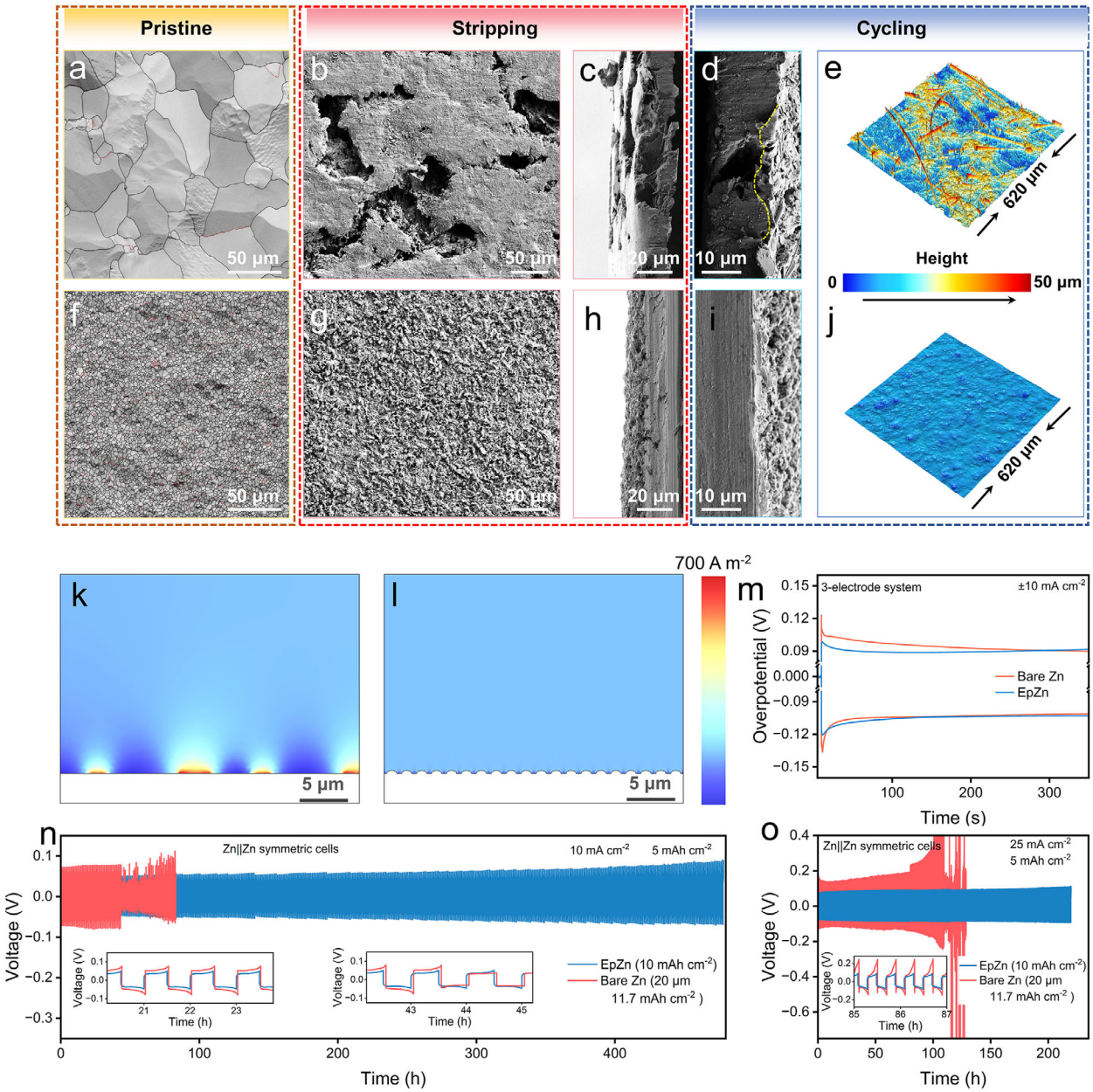

FIGURE 3 | Investigation of the intrinsic correlation between grain boundary distribution and cycling performance. (a–e) Characterization of commercial 20 μm Zn foils: (a) grain boundary distribution, (b) surface and (c) cross-sectional SEM images after stripping for 3 mAh cm^{-2} at 10 mA cm^{-2}, (d) cross-sectional SEM images and (e) LSCM image after 10 cycles at 10 mA cm^{-2} for 3 mAh cm^{-2}. (f–j) Characterization of EpZn electrodes: (f) grain boundary distribution, (g) surface and (h) cross-sectional SEM images after stripping 3 mAh cm^{-2} at 10 mA cm^{-2}, (i) cross-sectional SEM images and (j) LSCM image after 10 cycles at 10 mA cm^{-2} for 3 mAh cm^{-2}. (k,l) Simulated local current density distribution during stripping for (k) commercial Zn foils and (l) EpZn. (m) Chronopotentiometry tests conducted in a three-electrode system. (n,o) The cyclic performance of Zn||Zn symmetric cells at (n) 10 mA cm^{-2}, 5 mAh cm^{-2} and (o) 25 mA cm^{-2}, 5 mAh cm^{-2}.

tion in stabilizing Zn stripping and enabling long-term cycling stability.

2.3 | Implementation of Dynamic Gas Management via a Selective H_2-Expulsion Window

At the electrode level, the electrodeposition method thoroughly reconstructs the grain boundaries of the Zn anode, effectively mitigating short-circuit issues caused by dendrite penetration during short-term cycling. However, this approach does not alter the HER behavior on the Zn anode surface (Figure S17). Conventional pouch cell designs often reserve a gas chamber to accommodate the gaseous by-products generated during cycling and to prevent mechanical rupture. In aqueous systems, however, substantial gas evolution causes continuous and uncontrollable expansion of this chamber. As shown in Figure 4b, an EpZn||I_2 pouch cell with a reserved gas chamber accumulates more than 40 mL of gas after 1000 cycles, over twice the volume of the cell itself, which severely compromises volumetric energy density

15214095, 2026, 45, Downloaded from https://advanced.onlinelibrary.wiley.com/doi/10.1002/adma.73914 by Xiamen University, Wiley Online Library on [08/11/2026]. See the Terms and Conditions (https://onlinelibrary.wiley.com/terms-and-conditions) on Wiley Online Library for rules of use; OA articles are governed by the applicable Creative Commons License

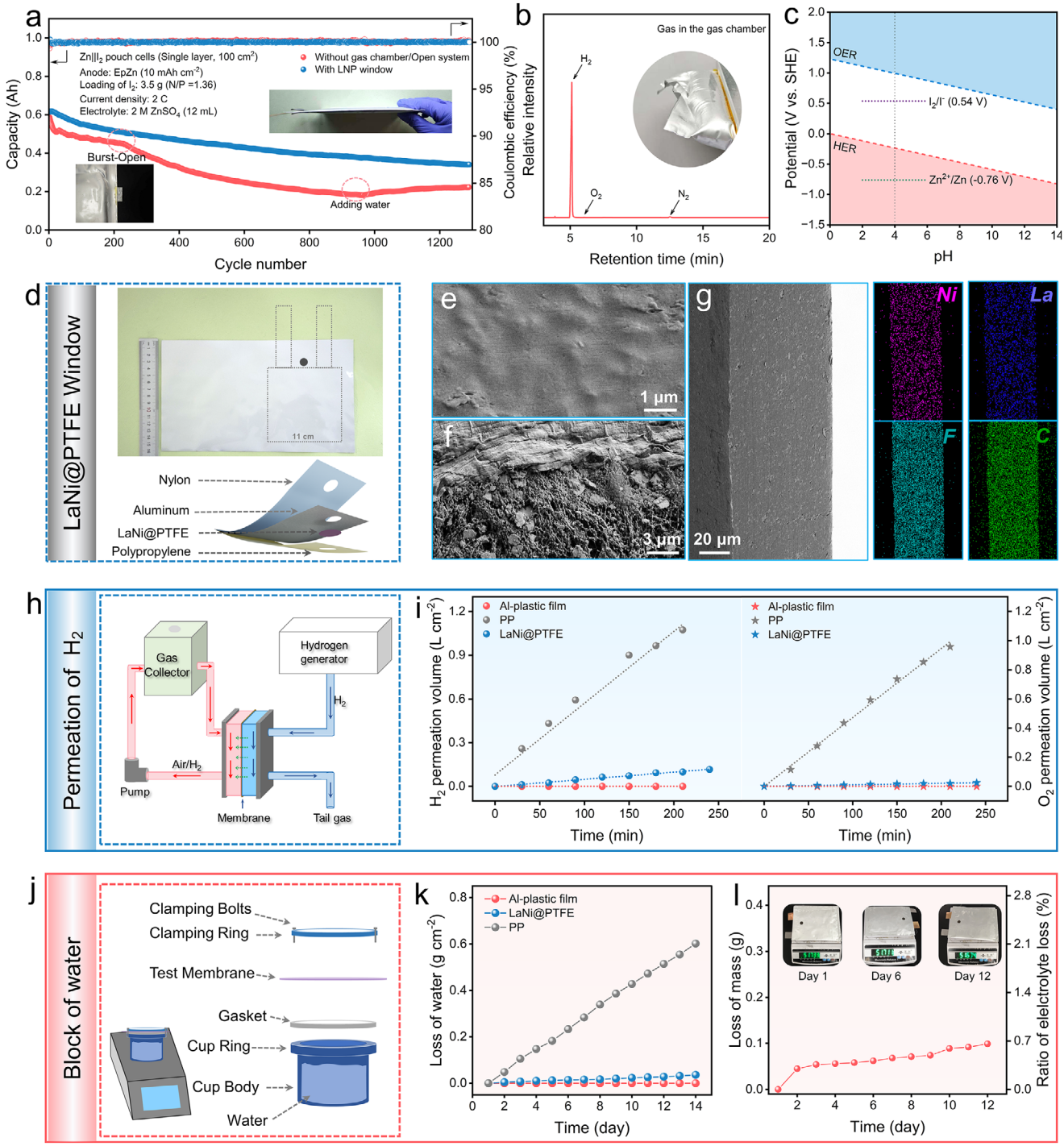

FIGURE 4 | Design of LaNi@PTFE selective H_2-expulsion window. (a) The cyclic performance of EpZn||I_2 pouch cells with/without LaNi@PTFE windows. (Inset is the corresponding photo of cycled cells). (b) Photograph of the swollen gas chamber in a cycled EpZn||I_2 pouch cell and corresponding gas chromatography analysis. (c) Pourbaix diagram of water. (d) Photograph and schematic diagram of the LaNi@PTFE window integrated into the Al-plastic film. (e,f) SEM images of the LaNi@PTFE film: (e) surface morphology and (f) local microstructure after tensile tearing. (g) Cross-sectional SEM image and corresponding elemental mappings of the LaNi@PTFE film. (h,i) The gas permeation test: (h) schematic of the setup and (i) H_2/O_2 permeation results for different membranes. (j–l) The water vapor transmission tests: (j) schematic diagram and (k) measured water vapor transmission rates for different membranes. (l) Water vapor barrier performance of the LaNi@PTFE window in an Ah-level EpZn||I_2 pouch cell under ambient conditions.

and hinders practical application. In the absence of such a gas chamber, even trace amounts of trapped gas accumulating at sealing points with relatively weak adhesion (e.g., electrode tab regions) can lead to pouch rupture, electrolyte leakage, and tab corrosion (Figure 4a). On the other hand, adopting an "open" cell configuration can alleviate internal pressure, but the continuous loss of electrolyte results in rapid capacity fading (Figure 4a). Gas chromatography (GC) analysis confirms that the evolved gas consists almost entirely of hydrogen, with only trace amounts of residual air from the cell assembly procedure (Figure 4b).

15214095, 2026, 45, Downloaded from https://advanced.onlinelibrary.wiley.com/doi/10.1002/adma.73914 by Xiamen University, Wiley Online Library on [08/11/2026]. See the Terms and Conditions (https://onlinelibrary.wiley.com/terms-and-conditions) on Wiley Online Library for rules of use; OA articles are governed by the applicable Creative Commons License

According to the Pourbaix diagram of water (Figure 4c), within the operating pH range (2–6) of Zn-I_2 batteries, the I_2/I^- redox potential lies above the HER potential but below that of oxygen evolution, while the zinc deposition potential is below the HER potential, explaining the predominance of hydrogen in the gas chamber. Therefore, mitigating hydrogen accumulation is essential for ensuring long-term cycling stability in aqueous Zn-I_2 pouch cells.

The existing strategies to suppress HER generally focus on kinetic inhibition through various interfacial approaches, such as replacing Zn with metals having higher HER overpotentials [48], regulating the solvation structure [49], disrupting the hydrogen-bond network [50, 51], and constructing protective layers that physically block water [52]. However, the thermodynamically favored HER is nearly inevitable during Zn plating. Given that, the gas accumulation problem in pouch cells is chosen to be addressed at the "device level" by integrating a selective H_2-expulsion window into the pouch cell packaging. Specifically, inspired by the absorption-desorption mechanism of hydrogen storage alloys, a selective hydrogen-expulsion window (LaNi@PTFE, LNP) was developed for the continuous removal of H_2 that is periodically generated during the charging process [53, 54], thus enabling the dynamic gas management.

The LaNi@PTFE film is fabricated by embedding $LaNi_5$ hydrogen-storage alloy nanoparticles (PDF#00-050-0777, Figure S18) into a hydrophobic PTFE matrix through a scalable roll-to-roll fabrication process. Tensile testing (Figure S19) demonstrates that the resulting LaNi@PTFE film is highly flexible, sustaining strains exceeding 20%. Importantly, the flexible LaNi@PTFE film can be incorporated into the aluminum-plastic film structure using standard Al-plastic film lamination processes, with negligible impact on the overall quality of the aluminum-plastic film (Figure S20). Consequently, the LaNi@PTFE layer is positioned between a pre-perforated aluminum layer and the inner polypropylene (PP) sealing layer, forming a functional Al-plastic film equipped with the LaNi@PTFE window (Figure 4d) for the subsequent direct assembly of 10 cm × 10 cm pouch cells. As shown in Figure 4e, the surface of the LaNi@PTFE film comprises a dense PTFE layer after repeated calendering and thermal pressing, with surface topography reflecting the underlying filler structure. The PTFE-rich surface endows the window with excellent hydrophobicity (Figure S21), forming a barrier that effectively blocks liquid electrolyte and water vapor. Besides, the local structure of LaNi@PTFE exposed by tensile tearing (Figure 4f) reveals a fibrillated PTFE network with LaNi particles embedded in the interstitial spaces. Cross-sectional SEM image (Figure 4g) further confirms a compact, uniform structure with homogeneous distribution of C/F (from PTFE) and La/Ni (from the LaNi alloy) elements.

The selective hydrogen expulsion capability of the LaNi@PTFE window was evaluated against two control samples: conventional Al-plastic film and a porous PP membrane (Celgard, a lithium-ion battery separator). Gas diffusion tests were performed in a custom-designed diffusion cell (Figure 4h and Figure S22), where pure H_2 or O_2 is introduced into one chamber, and permeation into the opposite chamber (diluted with air) is quantified using GC. As presented in Figure 4i and Figure S23, the PP membrane exhibits a leakage-level H_2 permeation rate (~295 mL h^{-1} cm^{-2}), whereas the aluminum-plastic film is completely hermetic with no gas permeation. In contrast, the LaNi@PTFE window shows a considerable H_2 permeation of 29.5 mL h^{-1} cm^{-2}, indicating controlled diffusion. Besides, oxygen tests yield a similarly high O_2 permeation rate for the PP membrane (~284 mL h^{-1} cm^{-2}), while the aluminum-plastic film remains impermeable (Figure 4i and Figure S24). Notably, the LaNi@PTFE window exhibits a much lower O_2 permeation rate of 6.2 mL h^{-1} cm^{-2}, only 1/5 of its H_2 permeation rate. Therefore, it can be speculated that the gases diffuse outward through the porous structure of PTFE, with the majority being blocked by the LaNi alloy within the voids, while a small portion may leak through the gaps. The LaNi alloy selectively absorbs H_2 and then desorbs it toward the external region of lower concentration, thereby achieving selective expulsion of hydrogen (Figure 1b).

Furthermore, the water vapor barrier performance was assessed using a water vapor transmission rate cup (Figure 4j and Figure S25). As shown in Figure 4k, after two weeks, the PP membrane control showed a significant water loss of 0.6 g cm^{-2} (Figure S26), whereas the pure Al-plastic film remained impermeable (Figure S27). The LaNi@PTFE window exhibited minimal water loss of only 0.036 g cm^{-2} (Figure S28). A single-layer Ep Zn||I_2 pouch cell (0.5 Ah) fabricated with the integrated H_2-expulsion-window-equipped film demonstrates only 0.5% electrolyte weight loss over 10 days after stabilization (Figure 4l), confirming the window's effectiveness in blocking electrolyte vapor loss.

The functional synergy between PTFE and the $LaNi_5$ alloy endows the LaNi@PTFE window with H_2-permeable and water-blocking capability. More importantly, the flexibility and hydrophobicity of PTFE significantly enhance the long-term stability and electrolyte resistance of the LaNi@PTFE window. After prolonged H_2 permeation aging, XRD analysis (Figure S29) and surface morphology characterization reveal no noticeable changes in the window (Figure S30). The H_2 permeation rate and water-vapor barrier performance remain nearly identical to the LaNi@PTFE pristine window (Figures S32 and S33), which can be attributed to the reversible hydrogen absorption/desorption nature of $LaNi_5$ (Figure S31), as well as the PTFE's flexibility for accommodating the potential volume expansion. Furthermore, even after immersion in the electrolyte, the strong hydrophobicity of PTFE effectively prevents electrolyte penetration into the interior, leaving the window surface morphology unchanged (Figure S34), with negligible impurity peaks in XRD patterns (Figure S29), and no significant variation in gas permeation or water-vapor barrier properties (Figures S35 and S36). These results confirm the excellent stability and anti-aging capability of the LaNi@PTFE window, ensuring its reliable operation over extended cycling. Moreover, the Ep Zn||I_2 pouch cell equipped with the LaNi@PTFE window eliminates the need for a reserved gas chamber; despite its more compact structure, it still maintains stable cycling for over 1200 cycles without observable swelling (Figure 4a and Figure S37), thereby validating the LaNi@PTFE window as an effective solution for mitigating hydrogen-induced swelling in practical pouch cells.

15214095, 2026, 45, Downloaded from https://advanced.onlinelibrary.wiley.com/doi/10.1002/adma.73914 by Xiamen University, Wiley Online Library on [08/11/2026]. See the Terms and Conditions (https://onlinelibrary.wiley.com/terms-and-conditions) on Wiley Online Library for rules of use; OA articles are governed by the applicable Creative Commons License

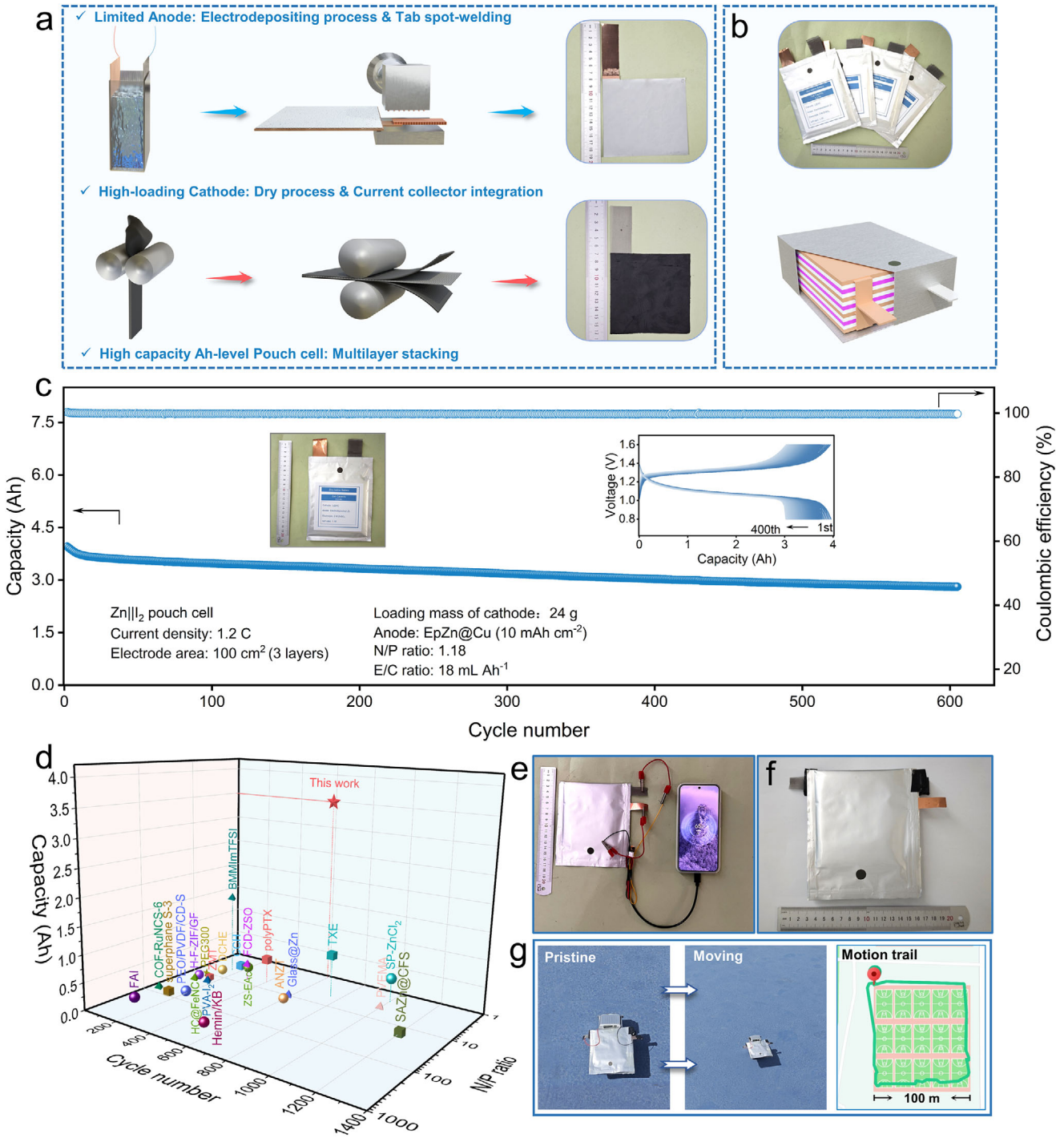

FIGURE 5 | Practical application of the integrated strategy in multilayer-stacking pouch cells. (a,b) Multilayer-stacking pouch cell assembly: (a) schematic and photograph of the manufactured electrodes; (b) schematic and photograph of multilayer-stacking Ah-level pouch cells. (c,d) (c) Cyclic performance of a 3.3 Ah multilayer-stacking EpZn||I_2 pouch cell, and (d) the performance comparison with reported Zn-I_2 pouch cells. (e–g) Demonstrations in real-devices: (e) Photograph of EpZn||I_2 pouch cell charging a mobile phone using a boost converter. (f) Photograph of four EpZn||I_2 pouch cells connected in series. (g) An electric toy car driven by the series-connected cells, with the motion trajectory illustrated in the inset.

2.4 | Application in Practical Multilayer-Stacking Pouch Cells

To further validate the practical applicability of this integrated electrode-to-device strategy, high-capacity pouch cells (>3 Ah) were fabricated via a multilayer stacking process. As presented in Figure 5a, the anode is an EpZn electrode with controllable capacity and reconfigured grain boundaries, incorporating an integrated Cu current collector. The stacked Cu collectors are connected via spot welding to a 50 μm-thick copper tab to ensure robust current conduction. On the cathode side, self-supporting iodine electrodes prepared by a dry process are roll-pressed onto

15214095, 2026, 45, Downloaded from https://advanced.onlinelibrary.wiley.com/doi/10.1002/adma.73914 by Xiamen University, Wiley Online Library on [08/11/2026]. See the Terms and Conditions (https://onlinelibrary.wiley.com/terms-and-conditions) on Wiley Online Library for rules of use; OA articles are governed by the applicable Creative Commons License

both sides of a Ti mesh current collector. Using a multilayer configuration consisting of 3 double-sided iodine cathodes, 6 EpZn anodes, and 6 separators, all encapsulated within an H_2-expulsion-window-equipped Al-plastic pouch film, 3 Ah-level pouch cells can be batch-produced (Figure 5b). As presented in Figure 5c, the assembled EpZn||I_2 pouch cell can deliver an initial discharge capacity of nearly 4 Ah and an average capacity of 3.3 Ah for over 600 stable cycles. Notably, this is achieved under ultrahigh cathode loading (>40 mg cm^{-2} per side) and an exceptionally low N/P ratio of 1.18, corresponding to a 66% DOD for the anode. This level of comprehensive performance compares favorably with many reported Zn-I_2 pouch cells (Figure 5d and Table S2). Considering the potential for mechanical damage in practical application scenarios, the window can be further protected by a gas-permeable yet mechanically tough protective layer (Figure S38). The practical utility of the system was validated through real-device demonstrations. A single pouch cell was able to charge a smartphone using a boost converter (Figure 5e and Video S3). Besides, a four-cell series configuration successfully powered an electric toy car for over 400 meters (Figure 5f,g and Video S4), underscoring the real-world viability of the proposed integrated strategy.

3 | Conclusions

In summary, this work identifies two scale-amplified failure mechanisms that dominate the performance degradation of Zn-I_2 batteries when transitioning from coin cells to Ah-level pouch cells. These two failure modes operate on different timescales and originate at different levels of the cell: early short circuits induced by heterogeneous grain boundaries in commercial Zn foil (an electrode-intrinsic issue), and persistent swelling and electrolyte leakage caused by H_2 accumulation over extended cycling (a device-level packaging issue). To address these distinct but interconnected challenges, we propose an integrated electrode-to-device design that couples two orthogonal strategies: grain-boundary reconstruction via scalable electrodeposition and a selective H_2-expulsion window integrated into the pouch packaging, thereby bridging the gap between electrode engineering and device-level functionality. Moreover, since this design operates at the electrode/device levels, which are distinct from conventional interface-level strategies for Zn anode modification, it is upwardly compatible with existing approaches (e.g., protective layers, electrolyte additives, or cathode modifications), offering a system-level, scalable pathway toward practical high-energy aqueous Zn-based pouch cells.

Acknowledgements

The authors gratefully acknowledge the financial support from the National Natural Science Foundation of China (Nos. 22579141 and 22379125), Fundamental Research Funds for the Central Universities (No. 20720250114). The authors acknowledge the Tan Kah Kee Innovation Laboratory for the help of scientific tests.

Funding

National Natural Science Foundation of China (Nos. 22579141 and 22379125), Fundamental Research Funds for the Central Universities (No. 20720250114)

Conflicts of Interest

The authors declare no conflicts of interest.

Data Availability Statement

The data that support the findings of this study are available on request from the corresponding author. The data are not publicly available due to privacy or ethical restrictions.

References

1. S. W. D. Gourley, R. Brown, B. D. Adams, and D. Higgins, "Zinc-Ion Batteries for Stationary Energy Storage," *Joule* 7 (2023): 1415–1436, https://doi.org/10.1016/j.joule.2023.06.007.

2. L. Tang, H. Peng, J. Kang, et al., "Zn-Based Batteries for Sustainable Energy Storage: Strategies and Mechanisms," *Chemical Society Reviews* 53 (2024): 4877–4925, https://doi.org/10.1039/D3CS00295K.

3. C. Li, S. Jin, L. A. Archer, and L. F. Nazar, "Toward Practical Aqueous Zinc-Ion Batteries for Electrochemical Energy Storage," *Joule* 6 (2022): 1733–1738, https://doi.org/10.1016/j.joule.2022.06.002.

4. H. Chen, X. Li, K. Fang, H. Wang, J. Ning, and Y. Hu, "Aqueous Zinc-Iodine Batteries: from Electrochemistry to Energy Storage Mechanism," *Advanced Energy Materials* 13 (2023): 2302187, https://doi.org/10.1002/aenm.202302187.

5. C.-C. Kao, C. Ye, J. Hao, Y. Chen, S.-J. Zhang, and S.-Z. Qiao, "Achieving High Energy Density in Aqueous Zinc-Ion Batteries," *Advanced Energy Materials* 15 (2025): 2501201, https://doi.org/10.1002/aenm.202501201.

6. K. Zhu, W. Xie, and W. Yang, "Aqueous Zinc-Ion Pouch Cells: from Failure Mechanisms to Practical Solutions," *Angewandte Chemie International Edition* 64 (2025): 202516233, https://doi.org/10.1002/anie.202516233.

7. H. Liu, X. Sun, X.-B. Cheng, et al., "Working Principles of Lithium Metal Anode in Pouch Cells," *Advanced Energy Materials* 12 (2022): 2202518, https://doi.org/10.1002/aenm.202202518.

8. C. Xu, B. Peng, W. Yang, J. Tian, and H. Zhou, "High Energy Density Lithium Battery Systems: from Key Cathode Materials to Pouch Cell Design," *Chemical Society Reviews* 54 (2025): 10245–10303, https://doi.org/10.1039/D5CS00641D.

9. S. Guo, M. Yao, S. Liang, and G. Fang, "Failure Mechanisms and Practical Optimizations for Ah-Scale Aqueous Zinc-Ion Pouch Cells," *Advanced Materials* 37 (2025): 12364, https://doi.org/10.1002/adma.202512364.

10. Y. Wang, T. Wang, S. Bu, et al., "Sulfolane-Containing Aqueous Electrolyte Solutions for Producing Efficient Ampere-Hour-Level Zinc Metal Battery Pouch Cells," *Nature Communications* 14 (2023): 1828, https://doi.org/10.1038/s41467-023-37524-7.

11. H. Wu, S.-J. Zhang, J. Vongsvivut, M. Jaroniec, J. Hao, and S.-Z. Qiao, "Aqueous Zinc-Iodine Batteries with Ultra-High Loading and Advanced Performance," *Joule* 9 (2025): 102000, https://doi.org/10.1016/j.joule.2025.102000.

12. C. Sun, M. Zhang, H. Xu, et al., "Scalable Roll-to-Roll Dry Processing of 10 mAh cm^{-2} Iodine Cathodes for Establishing Ah-Level Aqueous Zn–I_2 Pouch Cell Evaluation Protocol: Bridging Laboratory Research and Industrial Application," *Angewandte Chemie International Edition* 65 (2025): 17732, https://doi.org/10.1002/anie.202517732.

13. J. Guo, Z. Zhang, F. Zhu, Q. Yang, Y. Fu, and W. Guo, "Aqueous Zinc–Organoiodine Battery with High Kinetics and Dense Cathodes," *Journal of the American Chemical Society* 147 (2025): 39652–39661, https://doi.org/10.1021/jacs.5c13131.

14. M. Zhang, C. Sun, G. Chen, et al., "Synergetic Bifunctional Cu-In Alloy Interface Enables Ah-Level Zn Metal Pouch Cells," *Nature Communications* 15 (2024): 9455, https://doi.org/10.1038/s41467-024-53831-z.

15. Y. Song, M. Chen, Z. Zhong, Z. Liu, S. Liang, and G. Fang, "Bilateral in-Situ Functionalization towards Ah-Scale Aqueous Zinc Metal Batteries,"

15214095, 2026, 45, Downloaded from https://advanced.onlinelibrary.wiley.com/doi/10.1002/adma.73914 by Xiamen University, Wiley Online Library on [08/11/2026]. See the Terms and Conditions (https://onlinelibrary.wiley.com/terms-and-conditions) on Wiley Online Library for rules of use; OA articles are governed by the applicable Creative Commons License

Nature Communications 16 (2025): 3142, https://doi.org/10.1038/s41467-025-58153-2.

16. M. Zhang, S. Li, R. Tang, et al., "Stabilizing Zn/Electrolyte Interphasial Chemistry by a Sustained-Release Drug Inspired Indium-Chelated Resin Protective Layer for High-Areal-Capacity Zn//V_2O_5 Batteries," *Angewandte Chemie International Edition* 63 (2024): 202405593, https://doi.org/10.1002/anie.202405593.

17. Y. Zou, X. Yang, L. Shen, et al., "Emerging Strategies for Steering Orientational Deposition toward High-performance Zn Metal Anodes," *Energy & Environmental Science* 15 (2022): 5017–5038, https://doi.org/10.1039/d2ee02416k.

18. Z. Cao, P. Zhuang, X. Zhang, M. Ye, J. Shen, and P. M. Ajayan, "Strategies for Dendrite-Free Anode in Aqueous Rechargeable Zinc Ion Batteries," *Advanced Energy Materials* 10 (2020): 2001599, https://doi.org/10.1002/aenm.202001599.

19. N. Dong, F. Zhang, and H. Pan, "Towards the Practical Application of Zn Metal Anodes for Mild Aqueous Rechargeable Zn Batteries," *Chemical Science* 13 (2022): 8243–8252, https://doi.org/10.1039/d2sc01818g.

20. X. Huang, T. Pan, B. Zhang, et al., "Functionally Segregated Ion Regulation Enables Dual Confinement Effect for Highly Stable Zinc-Iodine Batteries," *Advanced Materials* 37 (2025): 2500500, https://doi.org/10.1002/adma.202500500.

21. H. J. Yang, Y. Qiao, Z. Chang, et al., "Reducing Water Activity by Zeolite Molecular Sieve Membrane for Long-Life Rechargeable Zinc Battery," *Advanced Materials* 33 (2021): 2102415, https://doi.org/10.1002/adma.202102415.

22. C. Yang, P. Woottapanit, S. Geng, et al., "A Multifunctional Quasi-Solid-State Polymer Electrolyte with Highly Selective Ion Highways for Practical Zinc Ion Batteries," *Nature Communications* 16 (2025): 183, https://doi.org/10.1038/s41467-024-55656-2.

23. X. Li, W. Zhang, J. Yu, et al., "Self-Assembled Protection Layer Induced by Bifunctional Additive for Reversible Aqueous Zinc Metal Battery," *Advanced Functional Materials* 34 (2024): 2316474, https://doi.org/10.1002/adfm.202316474.

24. Z. Wu, S. Yang, Z. Wei, et al., "Constructing Lipid-Like Biomimetic Structure via Electrolyte Designation for Stable Zinc-Ion Batteries," *ACS Nano* 19 (2025): 14085–14096, https://doi.org/10.1021/acsnano.4c18796.

25. Y. Guo, C. Luo, M. Yang, et al., "Dynamic Covalent Bonds Regulate Zinc Plating/Stripping Behaviors for High-Performance Zinc Ion Batteries," *Angewandte Chemie International Edition* 63 (2024): 202406597, https://doi.org/10.1002/anie.202406597.

26. Z. Liu, G. Li, M. Xi, et al., "Interfacial Engineering of Zn Metal via a Localized Conjugated Layer for Highly Reversible Aqueous Zinc Ion Battery," *Angewandte Chemie International Edition* 63 (2024): 202319091, https://doi.org/10.1002/anie.202319091.

27. L. Cao, D. Li, T. Pollard, et al., "Fluorinated Interphase Enables Reversible Aqueous Zinc Battery Chemistries," *Nature Nanotechnology* 16 (2021): 902–910, https://doi.org/10.1038/s41565-021-00905-4.

28. D. Xu, Z. Wang, C. Liu, et al., "Water Catchers within Sub-Nano Channels Promote Step-by-Step Zinc-Ion Dehydration Enable Highly Efficient Aqueous Zinc-Metal Batteries," *Advanced Materials* 36 (2024): 2403765, https://doi.org/10.1002/adma.202403765.

29. P. Ruan, X. Chen, L. Qin, et al., "Achieving Highly Proton-Resistant Zn–Pb Anode through Low Hydrogen Affinity and Strong Bonding for Long-Life Electrolytic Zn//MnO_2 Battery," *Advanced Materials* 35 (2023): 2300577, https://doi.org/10.1002/adma.202300577.

30. J.-L. Yang, T. Xiao, T. Xiao, et al., "Cation-Conduction Dominated Hydrogels for Durable Zinc–Iodine Batteries," *Advanced Materials* 36 (2024): 2313610, https://doi.org/10.1002/adma.202313610.

31. Z. Yang, C. Hu, Q. Zhang, et al., "Bulk-Phase Reconstruction Enables Robust Zinc Metal Anodes for Aqueous Zinc-Ion Batteries," *Angewandte Chemie International Edition* 62 (2023): 202308017, https://doi.org/10.1002/anie.202308017.

32. R. Guo, X. Liu, K. Ni, et al., "Non-Destructive Stripping Electrochemistry Enables Long-Life Zinc Metal Batteries," *Energy & Environmental Science* 18 (2025): 2353–2364, https://doi.org/10.1039/D4EE05044D.

33. S. Lian, Z. Cai, M. Yan, et al., "Ultra-High Proportion of Grain Boundaries in Zinc Metal Anode Spontaneously Inhibiting Dendrites Growth," *Angewandte Chemie International Edition* 63 (2024): 202406292, https://doi.org/10.1002/anie.202406292.

34. P. J. E. Forsyth, R. King, G. J. Metcalfe, and B. Chalmers, "Grain Boundaries in Metals," *Nature* 158 (1946): 875–876, https://doi.org/10.1038/158875a0.

35. Y. Zhao, S. Guo, M. Chen, et al., "Tailoring Grain Boundary Stability of Zinc-Titanium Alloy for Long-Lasting Aqueous Zinc Batteries," *Nature Communications* 14 (2023): 7080, https://doi.org/10.1038/s41467-023-42919-7.

36. Q. Li, A. Chen, D. Wang, et al., "Tailoring the Metal Electrode Morphology via Electrochemical Protocol Optimization for Long-Lasting Aqueous Zinc Batteries," *Nature Communications* 13 (2022): 3699, https://doi.org/10.1038/s41467-022-31461-7.

37. H. Gan, H. Li, M. Xu, C. Han, and H.-M. Cheng, "Failure Mechanisms and Remedy of an Ultrathin Zn Metal Anode in Pouch Cells," *Joule* 8 (2024): 3054–3071, https://doi.org/10.1016/j.joule.2024.07.013.

38. Y. Hu, P. Wang, M. Li, Z. Liu, S. Liang, and G. Fang, "Challenges and Industrial Considerations towards Stable and High-Energy-Density Aqueous Zinc-Ion Batteries," *Energy & Environmental Science* 17 (2024): 8078–8093, https://doi.org/10.1039/D4EE03628J.

39. S.-J. Zhang, J. Hao, H. Wu, et al., "Toward High-Energy-Density Aqueous Zinc–Iodine Batteries: Multielectron Pathways," *ACS Nano* 18 (2024): 28557–28574, https://doi.org/10.1021/acsnano.4c10901.

40. M. Zhang, H. Hua, P. Dai, et al., "Dynamically Interfacial pH-Buffering Effect Enabled by N -Methylimidazole Molecules as Spontaneous Proton Pumps toward Highly Reversible Zinc-Metal Anodes," *Advanced Materials* 35 (2023): 2208630, https://doi.org/10.1002/adma.202208630.

41. J. Cui, X. Liu, Y. Xie, et al., "Improved Electrochemical Reversibility of Zn Plating/Stripping: a Promising Approach to Suppress Water-Induced Issues through the Formation of H-Bonding," *Materials Today Energy* 18 (2020): 100563, https://doi.org/10.1016/j.mtener.2020.100563.

42. J. Chen, W. Zhao, J. Jiang, et al., "Challenges and Perspectives of Hydrogen Evolution-Free Aqueous Zn-Ion Batteries," *Energy Storage Materials* 59 (2023): 102767, https://doi.org/10.1016/j.ensm.2023.04.006.

43. Y. He, Y. Liu, W. Shang, and P. Tan, "Hydrogen Bubble Evolution and Its Induced Mass Transfer on Zinc Electrodes in Alkaline and Neutral Media," *Nanoscale* 17 (2025): 8453–8465, https://doi.org/10.1039/D4NR05108D.

44. J. Yin, H. Lin, J. Shi, et al., "Lead-Carbon Batteries toward Future Energy Storage: from Mechanism and Materials to Applications," *Electrochemical Energy Reviews* 5 (2022): 2, https://doi.org/10.1007/s41918-022-00134-w.

45. F. Wang, J. Zhang, H. Lu, et al., "Production of Gas-Releasing Electrolyte-Replenishing Ah-Scale Zinc Metal Pouch Cells with Aqueous Gel Electrolyte," *Nature Communications* 14 (2023): 4211, https://doi.org/10.1038/s41467-023-39877-5.

46. Q. Ren, X. Tang, Y. Guo, et al., "Achieving the Dendrite-Free Zn Anode by Inducing the (101)-Preferred Electrodeposition of Zn Crystals," *Advanced Energy Materials* 15 (2025): 2403961, https://doi.org/10.1002/aenm.202403961.

47. Z. Liu, Z. Guo, L. Fan, et al., "Construct Robust Epitaxial Growth of (101) Textured Zinc Metal Anode for Long Life and High Capacity in Mild Aqueous Zinc-Ion Batteries," *Advanced Materials* 36 (2024): 2305988, https://doi.org/10.1002/adma.202305988.

15214095, 2026, 45, Downloaded from https://advanced.onlinelibrary.wiley.com/doi/10.1002/adma.73914 by Xiamen University, Wiley Online Library on [08/11/2026]. See the Terms and Conditions (https://onlinelibrary.wiley.com/terms-and-conditions) on Wiley Online Library for rules of use; OA articles are governed by the applicable Creative Commons License

48. P. Xiao, H. Li, J. Fu, et al., "An Anticorrosive Zinc Metal Anode with Ultra-Long Cycle Life over One Year," *Energy & Environmental Science* 15 (2022): 1638–1646, https://doi.org/10.1039/d1ee03882f.

49. K. Zhao, G. Fan, J. Liu, et al., "Boosting the Kinetics and Stability of Zn Anodes in Aqueous Electrolytes with Supramolecular Cyclodextrin Additives," *Journal of the American Chemical Society* 144 (2022): 11129–11137, https://doi.org/10.1021/jacs.2c00551.

50. J. Chen, Y. Shi, S. Zheng, et al., "Blocking Interfacial Proton Transport via Self-Assembled Monolayer for Hydrogen Evolution-Free Zinc Batteries," *Angewandte Chemie International Edition* 63 (2024): 202404825, https://doi.org/10.1002/anie.202404825.

51. G. Zhou, W. Ding, Y. Guan, et al., "Suppressing Hydrogen Evolution Reaction by Constructing Interfacial Proton Blocking Layer for Highly Reversible Zinc Anode," *Energy Storage Materials* 72 (2024): 103756, https://doi.org/10.1016/j.ensm.2024.103756.

52. Y. Yang, H. Hua, Z. Lv, et al., "Reconstruction of Electric Double Layer for Long-Life Aqueous Zinc Metal Batteries," *Advanced Functional Materials* 33 (2022): 2212446, https://doi.org/10.1002/adfm.202212446.

53. Y. Xu, W. Yang, P. Wang, et al., "Bulk-to-IHP Zn Interphase Engineering with Mannitol Additive Enables (002)-Textured Zn Plating with Suppressed Hydrogen Evolution Reaction for Ah-Level Aqueous Zinc-Iodine Pouch Cells," *Advanced Materials* 38 (2026): 18824, https://doi.org/10.1002/adma.202518824.

54. X. Yu, M. Chen, Z. Li, et al., "Unlocking Dynamic Solvation Chemistry and Hydrogen Evolution Mechanism in Aqueous Zinc Batteries," *Journal of the American Chemical Society* 146 (2024): 17103–17113, https://doi.org/10.1021/jacs.4c02558.

Supporting Information

Additional supporting information can be found online in the Supporting Information section.

Supporting File 1: adma73914-sup-0001-SuppMat.docx.

Supporting File 2: adma73914-sup-0002-VideoS1-S4.zip.

15214095, 2026, 45, Downloaded from https://advanced.onlinelibrary.wiley.com/doi/10.1002/adma.73914 by Xiamen University, Wiley Online Library on [08/11/2026]. See the Terms and Conditions (https://onlinelibrary.wiley.com/terms-and-conditions) on Wiley Online Library for rules of use; OA articles are governed by the applicable Creative Commons License